Nonlinear Breit-Wheeler pair production in collisions of bremsstrahlung γ quanta and a tightly focused laser pulse

A. Golub,[*] S. Villalba-Chávez,[†] and C. Müller[‡]

Institut für Theoretische Physik I, Heinrich-Heine-Universität Düsseldorf, Universitätsstraße 1, 40225 Düsseldorf, Germany

(Received 28 March 2022; accepted 25 May 2022; published 21 June 2022)

Experimental efforts toward the detection of the nonperturbative strong-field regime of the Breit-Wheeler pair creation process plan to combine incoherent sources of GeV γ quanta and the coherent fields of tightly focused optical laser pulses. This endeavor calls for a theoretical understanding of how the pair yields depend on the applied laser field profile. We provide estimates for the number of produced pairs in a setup where the high-energy radiation is generated via bremsstrahlung. Attention is paid to the role of the transversal and longitudinal focusing of the laser field, along with the incorporation of a Gaussian pulse envelope. We compare our corresponding results with predictions from plane-wave models and determine the parameters of focused laser pulses which maximize the pair yield at fixed pulse energy. Besides, the impact of various super-Gaussian profiles for the laser pulse envelope and its transverse shape is discussed.

DOI: 10.1103/PhysRevD.105.116016

I. INTRODUCTION

Materializing quantum vacuum fluctuations into real electron-positron pairs from collisions of photons is among the iconic predictions of quantum electrodynamics that support the contemporary perception of the quantum vacuum as a source of nonlinear electromagnetic interactions. In fact, theoretical studies that followed Breit and Wheeler's pioneering work on the linear pair production by two photons [1] revealed creation channels $\gamma' + n\gamma \to e^- + e^+$ in which n background photons could be absorbed simultaneously in the course of a single pair creation event [2–7]. This nonlinear landscape is expected to occur in both the perturbative weak-field ($\xi \ll 1$) and nonperturbative strong-field ($\xi \gg 1$) regimes ruled by the laser intensity parameter $\xi = |e\mathcal{E}_0|/(m\omega)$, characterized by the laser frequency ω and peak field strength $\mathcal{E}_0$.[1] In the former scenario the partial rates linked to nonlinear events $R_n \sim \xi^{2n}$ are suppressed as the number of absorbed photons ($n > 1$) grows. This means that—in practice—nonlinear Breit-Wheeler reactions in the field of a laser with $\xi < 1$ are likely to take place with the absorption of few photons only. The described scenario was confirmed experimentally by the SLAC E-144 collaboration [8]. Besides, by accelerating gold ions to ultra-relativistic energies, an experimental validation of the linear channel ($n = 1$) in collisions of quasireal photons has been reported recently [9].

In contrast to the perturbative scenario, a large amount of laser photons is predicted to be absorbed when a single pair is produced under the condition $\xi \gg 1$. So far this highly nonlinear regime lacks an experimental observation, mainly because the total production rate $R \sim \exp[-8/(3\kappa)]$, with $\kappa = 2\omega'\mathcal{E}_0/(mE_c)$ for counterpropagating beam geometry, is exponentially suppressed unless the effective peak field strength $(\omega'/m)\mathcal{E}_0$ comes close to the characteristic Schwinger scale $E_c = m^2/|e| \approx 1.3 \times 10^{16}$ V cm^{-1}. Here, ω' stands for the frequency of the weak field. While $\mathcal{E}_0$ as large as E_c is yet inaccessible in the laboratory frame, the possibility of producing highly energetic γ radiation ($\omega' \gtrsim \mathcal{O}(1)$ GeV) via bremsstrahlung combined with both the current availability of multi-petawatt laser facilities [10] and unprecedented detection techniques, makes the first confirmation of the nonperturbative strong-field regime of the Breit-Wheeler pair creation process come into reach. As a consequence, various experimental endeavors are being planned worldwide, including the projects E-320 at SLAC [11] and LUXE at DESY [12,13] as well as the upcoming experiments at the Rutherford Appleton Laboratory [14] and the one put forward by the Center of Advanced Laser Applications (CALA) [15].

Clearly, as the high-intensity lasers involved in the listed collaborations ($I \lesssim \mathcal{O}(10^{22})$ W cm^{-2}) are tightly focused

[*]Alina.Golub@uni-duesseldorf.de
[†]selym@tp1.uni-duesseldorf.de
[‡]c.mueller@tp1.uni-duesseldorf.de

[1]Throughout this paper we use Lorentz-Heaviside units where $c = \hbar = \epsilon_0 = 1$. Besides, the signature of the metric tensor is chosen with $\mathrm{diag}(g^{\mu\nu}) = (1, -1, -1, -1)$. The symbols e and m stand for the electron charge and mass, respectively.

and the production of γ quanta through bremsstrahlung generates a broad spectrum, attempts in describing theoretically the forthcoming measurements require to go beyond the traditional treatments of pair production by a monoenergetic γ beam and a plane-wave laser field, on which most of the investigations carried out so far rely [3–7,16–28]. This situation renders theoretical studies of the strong field pair production process in realistic setups a subject of raising interest. Although a comprehensive theoretical framework including the aforementioned properties is far from being accomplished, progresses toward understanding the role of the transversal focusing of the high-intensity laser pulse have been achieved at the fundamental level, where a single γ quantum of fixed energy intervenes [29–31]. Parallelly, there have been efforts for assessing the impact of the spectral distribution of bremsstrahlung γ quanta on the production of pairs by adopting various models for the strong background laser field [32–34].

The present manuscript aims to provide first estimates for the expected pair yields by including simultaneously both the focusing of the high-intensity laser pulse as well as the frequency spectrum and spatial spreading of the bremsstrahlung γ beam. We consider a modern version of the setup proposed originally by Reiss [6], in which a high-intensity optical laser field and high energy γ quanta—produced in the course of the interaction between highly energetic incident electrons and a thin high-Z target—collide, giving rise to electron-positron pairs (see Fig. 1).[2] The benchmark parameters used in our investigation are in correspondence with those envisaged in Ref. [15], which guarantee the realization of the nonperturbative strong-field regime ($\xi \gg 1$, $\kappa \sim 1$) of the Breit-Wheeler pair production process. In this parameter regime, a locally constant field approximation (LCFA) can be applied [7,36–40]. Its use allows us to assess the role of the transversal and longitudinal focusing of the laser field along with the incorporation of the Gaussian pulse envelope. We show that the inclusion of the spatial laser focusing reduces the pair production yield as compared to scenarios relying on plane-wave pulses comprising the same pulse energy and establish intensity-focusing parameters for which the number of production events is optimized. Besides, the impact of choosing super-Gaussian profiles for the pulse envelope and the transversal shape of the laser field is analyzed separately.

The manuscript is organized as follows. In Sec. II we provide details of the theoretical framework used in our analysis. Particularly, in Sec. II A various aspects of the bremsstrahlung γ radiation are introduced and some assumptions are adopted. We then proceed with Sec. II B, where some laser field profiles to be investigated are presented.

[2]A similar setup has been put forward as an alternative route for verifying the linear Breit-Wheeler reaction. The interested readers are referred to Ref. [35], where the associated phenomenology is discussed in detail.

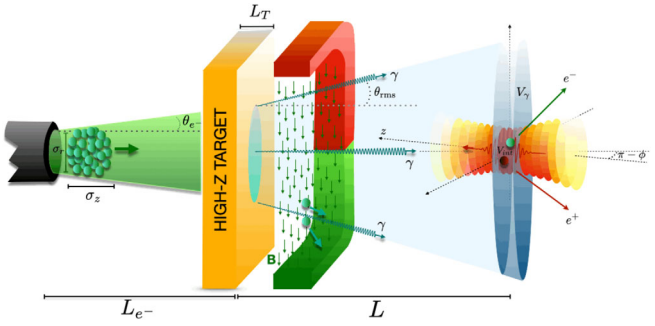

FIG. 1. Sketch of an experimental setup put forward to create e^-e^+-pairs from the collision of bremsstrahlung γ quanta and a tightly focused laser pulse in the nonperturbative strong-field regime ($\xi \gg 1$, $\kappa \sim 1$) of the Breit-Wheeler process. The high-Z target responsible for the generation of the γ radiation is supposed to be thin. A magnet is located right after the target to deflect primarily the electron flux that traverses it. The spreading beam of bremsstrahlung photons forms a cone colored in blue. For more details on the planned experiment we refer the reader to Ref. [15].

Next, in Sec. II C expressions for the production probability and the number of produced pairs per radiating electron are elucidated via LCFA. In parallel, an expression for the pair production rate in a constant crossed field is derived for the regime where the conditions $\xi \gg 1$ and $\kappa \approx 1$ are fulfilled simultaneously. The formulas obtained in Sec. II C are afterwards exploited to assess numerically the impact of the different laser field models. The results of these evaluations are discussed in Sec. III. While in Sec. III A comparisons between the constant crossed field, plane-wave and paraxial field models are carried out, Sec. III D is devoted to evaluate effects linked to super-Gaussian profiles. The role of different focal regions within the photo-production of pairs is studied in Sec. III B, whereas the impact of the relation between tighter focus and higher intensity is investigated in Sec. III C. Finally, in Sec. IV, we present our conclusion, whereas in the appendices details on the space-dependent quantum nonlinearity parameter are given and expressions for the electric field beyond the paraxial approximation are listed.

II. THEORETICAL APPROACH

The envisaged setup is split into two stages in which the generation of high-energy γ radiation and the pair production processes occur separately. While in the first stage, the γ quanta are produced through bremsstrahlung of an incident highly collimated beam of ultrarelativistic electrons, in the second stage a fraction of them collides with a high-intensity laser pulse. This section is devoted to introduce the analytical tools that are used in the description of the strong-field nonlinear Breit-Wheeler pair production as it may occur in the depicted configuration (see Fig. 1).

A. Bremsstrahlung spectrum

In our numerical computations, we shall consider incident electron beams comprising several pC of total charge which have reached an energy E_0 of few GeV via laser wake-field acceleration (LWFA). The spatial extent of such electron beams depends on the precise regime of acceleration. To be specific, we shall assume that the accelerating field needed for exciting the plasma wake is taken from the same laser source which provides the tightly focused laser pulse that drives the pair production process in the second stage, as it is experimentally planned [15]. However, in contrast to the latter pulse, the former will be weakly focused. The axial extension of the electron beam σ_z varies depending upon the plasma density $\mathfrak{n}_e < 10^{18}$ cm^{-3} and the parameters of the weakly focused laser wave. The experiment at CALA aims to prepare a monoenergetic bunch by the end of the acceleration process and this will occur if the electron beam is short enough to experience an approximately uniform accelerating field. This in turn takes place at distances smaller than the plasma wavelength $\lambda_\mathrm{p} = 2\pi\omega_\mathrm{p}^{-1}$ with $\omega_\mathrm{p} = (e^2\mathfrak{n}_e/m)^{1/2}$ referring to the plasma frequency. Indeed, in the blow-out regime of the LWFA $\mathfrak{n}_b > \mathfrak{n}_e$, with $\mathfrak{n}_b$ referring to the electron beam density, both the axial σ_z and radial σ_r extensions of the witness bunch are bound by $\sigma_{z,r} < \lambda_\mathrm{p}/(2\pi)$ [41–43]. Under such a circumstance, the beam spreading characterized by a broadening angle θ_{e^-} has been estimated to be of the order of $\theta_{e^-} \approx 0.5$ mrad, while the distance traveled by the electrons toward the high-Z target will be set to $L_{e^-} = 10$ cm.

Simulations carried out in Ref. [15] provide evidences that only ∼1% of the electrons in the beam will produce bremsstrahlung radiation. Upon penetrating a high-Z target with thickness L_T much smaller than the characteristic radiation length L_rad of the material [$L_\mathrm{T} \ll L_\mathrm{rad}$], the emission of bremsstrahlung photons takes place within the electron beam volume which undergoes almost no spatial spreading due to the ultrarelativistic nature of its constituents. Hence, we will assume that the longitudinal extension of the bremsstrahlung burst amounts to σ_z as well. In this context, the spreading angle of generated radiation can be approximated by the inverse electron Lorentz factor $\theta_\gamma \approx 1/\gamma_e = m/E_0 \sim \mathcal{O}(1)$ mrad. As a consequence the vast majority of the bremsstrahlung photons are emitted tangentially to the direction of propagation of the incident electron beam. The energy spectrum of bremsstrahlung photons, which are produced by electrons passing through a solid high-Z target, in the thin target approximation and complete screening case[3] reads [44,45]

$$I_\gamma(f,\ell) = E_0\frac{d\mathcal{N}_\gamma}{d\omega'} \approx \frac{\ell}{f}\left(\frac{4}{3} - \frac{4f}{3} + f^2\right), \tag{1}$$

where $\mathcal{N}_\gamma$ is the number of emitted photons by a radiating electron, $f = \omega'/E_0$ refers to the normalized photon energy of the emitted γ radiation and $\ell = L_\mathrm{T}/L_\mathrm{rad}$ denotes the normalized target thickness. In our numerical studies we shall assume a target made of tungsten for which the radiation length is $L_\mathrm{rad} = 3.5$ mm.

Unless stated otherwise, we use Eq. (1) throughout this study. However, we should mention at this point that another approximative formula for the bremsstrahlung spectrum is available in the literature [45] which, in contrast to Eq. (1), is well suited for thicker targets with $\ell < 2$:

$$I_\gamma(f,\ell) \approx \frac{(1-f)^{4\ell/3} - \mathrm{e}^{-7\ell/9}}{f(7/9 + 4/3\log(1-f))}. \tag{2}$$

We compare the outcomes from Eqs. (1) and (2) for $L_\mathrm{T} = 50\ \mu$m ($\ell = 0.015$) in Fig. 2. Here, the dashed red line accounts for the thin target approximation, whereas the blue solid holds for thicker targets. Both analytical models (1) and (2) are known to describe the spectrum of bremsstrahlung photons well (as, for example, the comparison with numerical GEANT4 simulations in [15,32] demonstrates), but show an unrealistic divergence in the infrared limit $f \to 0$. However, as we will see below, the low energetic part of the spectrum with $f \lesssim 0.2$ will practically not contribute to the pair creation in the envisaged parameter regime. Hence, the divergence is not harmful and the impact of this part of the spectrum may be neglected. Furthermore, the thin target approximation does not manifest the characteristic steep decrease at the point $f \approx 1$ stemming from the fact that no photons can be emitted with energy greater than the energy of the incident electrons. Also this region of the spectrum therefore needs to be considered with care. The

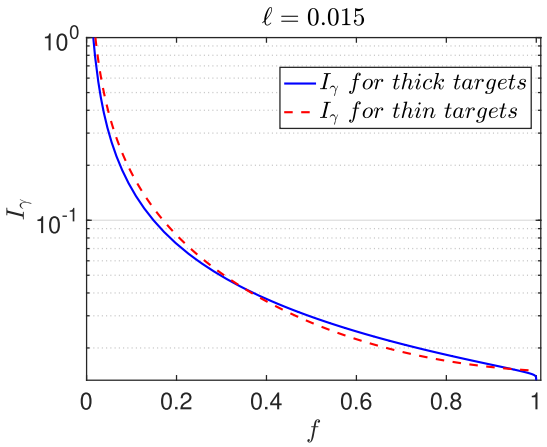

FIG. 2. Bremsstrahlung spectra according to Eqs. (1) (red dashed) and (2) (blue solid).

[3]In general, the bremsstrahlung spectrum depends on the atomic number Z of the target material. This is encoded in Eq. (1) via the radiation length L_rad. Additional $Z-$dependent terms have been ignored, though, which introduces a minor error of maximal 2.5% [44,45]. Moreover, "complete screening" refers to screening of nuclear Coulomb potentials by atomic electrons, which is particularly effective at high energies E_0 and small emission angles θ_γ.

contributions of incident electrons with different energies to the pair creation rate by considering separately thin and tick targets are studied at the beginning of Sec. III.

As described above, in the second stage the bremsstrahlung γ burst collides with a high-intensity laser pulse of optical frequency $\omega \sim \mathcal{O}(1)$ eV and large value of $\xi \gg 1$. The collision will take place at some distance $L \sim \mathcal{O}(1)$ m from the target under a collision angle ϕ between the bremsstrahlung beam and the strong laser pulse. Observe that, due to the spreading, the bremsstrahlung radiation covers a volume (see Fig. 1):

$$V_\gamma \approx \pi \sigma_z \bar{r}^2 \quad \text{with} \quad \bar{r} = \frac{r_{\min} + r_{\max}}{2} \tag{3}$$

the average radius of the truncated cone formed by the bremsstrahlung burst. Here, the maximal and minimal radii are $r_{\max} \approx \theta_{\rm rms}\sigma_z + r_{\min}$ and $r_{\min} = \sigma_r + L_{e^-}\theta_{e^-} + L\theta_{\rm rms}$, respectively with $\sigma_r < \lambda_{\rm p}/(2\pi)$ denoting the transversal extension of the witness beam and $\theta_{\rm rms} = (\theta_{e^-}^2 + \theta_\gamma^2)^{1/2}$ counting for the root-mean squared of the spreading angle. We note that, in the planned experiment at CALA, $\bar{r} \approx r_{\min} \approx L_{e^-}\theta_{e^-} + L\theta_{\rm rms} \approx 320\ \mu$m (see Ref. [15]).

B. Laser field profiles

The element of the setup that is left to be described is the high-intensity laser field which takes part in the second stage of the experiment. We will suppose this pulse background propagating along the $z-$axis with a linear polarization characterized by the vector $\boldsymbol{\epsilon} = (1,0,0)$. Consequently, the nontrivial electric field component to be specified is $E_x = B_y$. While in the course of our calculations various strong field profiles are analyzed, the field shape resulting from the paraxial approximation is adopted as a reference model [46]:

$$E_x = \mathcal{E}_0 \frac{\mathrm{e}^{-\left(\sqrt{2\ln(2)}\frac{(t-z)}{\tau}\right)^2}}{\sqrt{1+\zeta(z)^2}} \mathrm{e}^{-\left(\frac{r}{w(z)}\right)^2} \sin(\Phi). \tag{4}$$

Here, $w(z) = w_0\sqrt{1+\zeta(z)^2}$ stands for the beam width which depends on the longitudinal coordinate z via the factor $\zeta(z) = z/z_R$. In this context, $z_R = \pi w_0^2/\lambda$ is the Rayleigh length, whereas w_0 refers to the beam waist size at the focal point ($z = 0$). The nontrivial Gaussian dependence on $r^2 = x^2 + y^2$ accounts for the transversal behavior of the pulse, whereas its temporal extension τ is taken at FWHM from the intensity. Moreover, the pulse phase is

$$\Phi = \omega(t-z) - \zeta(z)\frac{r^2}{w^2(z)} + \arctan(\zeta). \tag{5}$$

The beam energy carried by this pulse, which in practice is fixed and does not change by focusing into various field profiles, can be calculated from the associated local power:

$$P(t,z) = \frac{\mathcal{E}_0^2}{2}\frac{\pi w_0^2}{2}\mathrm{e}^{-2\left(\sqrt{2\ln(2)}\frac{\varphi}{\omega\tau}\right)^2} \times \left\{1 - \frac{1}{1+\zeta(z)^2}\left[\cos(2\varphi) - \zeta(z)\sin(2\varphi)\right]\right\} \tag{6}$$

with $\varphi = \omega(t-z)$. Once the integration over time is carried out, one obtains the pulse energy

$$W_{\rm G} \approx \frac{\mathcal{E}_0^2}{2}\frac{\pi w_0^2}{2}\frac{\tau}{2}\sqrt{\frac{\pi}{\ln(2)}} \tag{7}$$

with the accuracy up to a term decreasing exponentially in $(\omega\tau)^2$, provided $\omega\tau \gg 1$. The expression above will be used to adjust the laser intensity and focusing parameters linked to other field models while keeping their energies equal to Eq. (7).

In addition to the previous focused Gaussian pulse, we shall adopt a description for the strong laser field which relies on a pulsed plane wave model. The field associated with this scenario can be read off from Eq. (4) when the limit $w_0 \to \infty$ is taken. Explicitly,

$$E_x(\varphi) = \mathcal{E}_0 \mathrm{e}^{-\left(\sqrt{2\ln(2)}\frac{\varphi}{\omega\tau}\right)^2}\sin(\varphi) \coloneqq \mathcal{E}_0\psi(\varphi). \tag{8}$$

In contrast to the paraxial approximation a plane wave is infinitely extended perpendicularly to the direction of propagation and as a consequence, the associated beam power would formally diverge. In order to perform a fair comparison, the infinite transversal beam area can be parametrized conveniently by $A_{\rm int}$. In such a scenario the instantaneous beam power results $P(\varphi) = E_x^2(\varphi)A_{\rm int}$ and the corresponding energy carried by the beam reads

$$W_{\rm pw} \approx \frac{\mathcal{E}_0^2}{2}A_{\rm int}\frac{\tau}{2}\sqrt{\frac{\pi}{\ln(2)}}. \tag{9}$$

A comparison with Eq. (7) allows us to identify the effective interacting area $A_{\rm int} = \pi w_0^2/2$. Implicitly, this means that the strong field is truncated transversally, i.e. $E_x(\varphi) \to E_x(\varphi)\Theta(r)\Theta(w_0/\sqrt{2} - r)$ with $\Theta(x)$ denoting the unit step function. Observe that in the limit $\omega\tau \to \infty$ the plane wave in Eq. (8) becomes monochromatic with a power $P(\varphi) = \mathcal{E}_0^2\sin^2(\varphi)A_{\rm int}$. In this context, the beam energy equals $W_{\rm mpw} = \langle P\rangle T_{\rm int}$, where $\langle P\rangle = IA_{\rm int}$ is its mean power with $I = \mathcal{E}_0^2/2$ referring to the time-averaged intensity. Upon a comparison between $W_{\rm mpw}$ and Eq. (9) we end up with $T_{\rm int} = \frac{\tau}{2}\sqrt{\frac{\pi}{\ln(2)}}$.

The procedure is extendable to paraxial pulses modulated by super-Gaussian profiles (see Fig. 3), which are characterized by higher powers within the time-dependent exponent of Eq. (4); i.e., when the power 2 there is replaced by $n = 4, 8, \ldots$ the field becomes

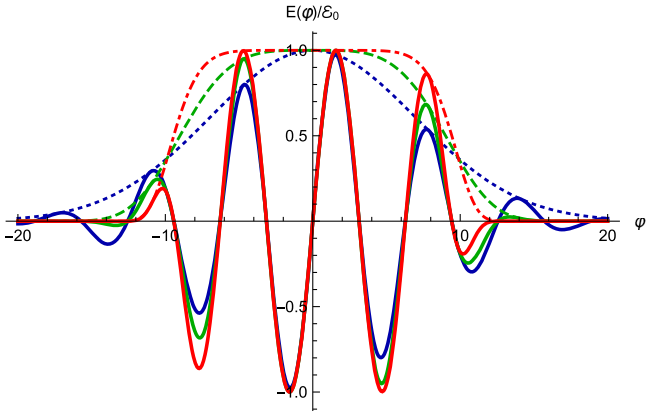

FIG. 3. Plane-wave pulses ($w_0 \to \infty$) with Gaussian and super-Gaussian-profiles with $n = 4$ and $n = 8$ are shown in blue, green and red, respectively. While the pure Gaussian envelope is dotted, the corresponding modulated functions linked to $n = 4$ and $n = 8$ are dashed and dot-dashed. These envelopes are given as references. This picture has been generated by setting $\tau = 5$ fs and $\omega = 1.55$ eV.

$$E_x = \mathcal{E}_0 \frac{e^{-\left(\sqrt{2\ln(2)}\frac{(t-z)}{\tau}\right)^n}}{\sqrt{1+\zeta(z)^2}} e^{-\left(\frac{r}{w(z)}\right)^2} \sin(\Phi). \tag{10}$$

Observe that, as n increases, the field profiles linked to super-Gaussian models acquire plateaus which enable to reach the peak intensity several times as compared to the case modulated by the standard Gaussian function. Likewise, the aforementioned growing of n reduces gradually the ramping (deramping) interval, making its slope steeper than in the Gaussian model. The corresponding energies for $n = 4$ and $n = 8$ are

$$W_{n=4} \approx \frac{\mathcal{E}_0^2}{2}\frac{\pi w_0^2}{2}\frac{\tau 2^{1/4}\Gamma(\frac{5}{4})}{\sqrt{\ln(2)}},$$
$$W_{n=8} \approx \frac{\mathcal{E}_0^2}{2}\frac{\pi w_0^2}{2}\frac{\tau 2^{3/8}\Gamma(\frac{9}{8})}{\sqrt{\ln(2)}} \tag{11}$$

with $\Gamma(x)$ denoting the Gamma function [47]. Observe that as long as we refer to a common laser system the peak intensity will vary when the pulse energy is kept fixed.

Super-Gaussian profiles can also be used when modeling the transverse shape of the wave. However, in contrast to the previous scenario, the intensity linked to these beams at the focal plane $z = 0$ is [48,49]

$$I(r) = I_0 e^{-2\left(\frac{r}{w_0}\right)^m} \tag{12}$$

with $m \geq 2$ and peak intensity $I_0 = \mathcal{E}_0^2$. Correspondingly, a pulse transversally focused by a super-Gaussian profile has a nonvanishing electromagnetic field component of the form

$$E_x = \mathcal{E}_0 e^{-\left(\sqrt{2\ln(2)}\frac{\varphi}{\omega\tau}\right)^2} e^{-\left(\frac{r}{w_0}\right)^m} \sin(\varphi). \tag{13}$$

For $m = 2$, the formula above describes the leading order term of the paraxial field [see Eq. (4)] in $z/z_R \ll 1$, which is a good approximation for the focal inner region. In the limit of $m \to \infty$ the transversal part tends to a rectangular function. The pulse energy for $m = 4$ and $m = 8$ results into

$$W_{m=4} \approx \frac{\mathcal{E}_0^2}{2}\frac{\pi^{3/2} w_0^2}{2^{3/2}}\frac{\tau}{2}\sqrt{\frac{\pi}{\ln(2)}},$$
$$W_{m=8} \approx \frac{\mathcal{E}_0^2}{2}\frac{\pi w_0^2 \Gamma(\frac{5}{4})}{2^{1/4}}\frac{\tau}{2}\sqrt{\frac{\pi}{\ln(2)}}. \tag{14}$$

We remark that an analytical expression for the transversal super-Gaussian beams does not exist outside the focal plane $z = 0$. Hence, Eq. (13) can only be applied when longitudinal focusing of the laser beam can be disregarded.

C. Pair creation by bremsstrahlung photons in a strong laser pulse within the locally constant field approximation

We shall suppose that the production process is dominated by the space-time region in which the strong field condition $\xi(\boldsymbol{x}, t) \gg 1$ holds. Under such circumstances the characteristic pair formation length $l \sim \lambda/(\xi\pi)$ turns out to be much smaller than $\lambda = 2\pi\omega^{-1}$, enabling an effective description in which the laser background can be treated locally as a constant field whose electric and magnetic field strengths are orthogonal and equal. This locally constant field approximation is applicable for low frequencies $\omega \ll m$ and large values of ξ starting from $\xi \gtrsim 5$, as it was shown in Ref. [50].

As a consequence, the local probability rate per unit of volume for producing a pair by a single bremsstrahlung γ photon can be approximated by [51,52]

$$\left.\frac{d\mathscr{P}}{dtdV}\right|_{\xi(\boldsymbol{x},t)\gg 1} \approx R(\kappa)|_{\xi\to\xi(\boldsymbol{x},t)}, \tag{15}$$

where $R(\kappa)$ is the transition rate per volume of the pair production process in a constant crossed field [3,4,7]:

$$R(\kappa) = -\frac{\alpha m^2}{6\sqrt{\pi}\omega' V_\gamma}\int_1^\infty \frac{du(8u+1)}{u\sqrt{u(u-1)}}\frac{\Phi'(z)}{z}. \tag{16}$$

Here $\kappa = kk'\xi/m^2$ denotes the quantum nonlinearity parameter with $k' = (\omega', \boldsymbol{k}')$ and $k = (\omega, \boldsymbol{k})$ referring to the corresponding four-momentum of the γ quanta and the laser wave. Observe that the local density rate depends on the derivative $\Phi'(z) = d\Phi/dz$ of the Airy function $\Phi(z) = \frac{1}{\sqrt{\pi}}\int_0^\infty dt \cos(\frac{t^3}{3} + zt)$ with argument $z = (4u/\kappa)^{2/3}$. We remark that the expression above applies as long as $\xi \gg \max\{1, \kappa^{1/3}\}$ holds and perturbation theory is still

valid, i.e., if the condition $\alpha\kappa^{2/3} < 1$ is fulfilled with $\alpha \approx 1/137$ referring to the fine structure constant [53–58].

In the following we shall assume that the mean collision angle between the bremsstrahlung burst and strong laser pulse is $\phi = \pi$. As we are interested in comparing the pair yields stemming from various external field models, we shall discuss in this section particularities of the corresponding expressions for the number of produced pairs per radiating electron:

$$N \approx \int_0^{E_0} d\omega' \langle \mathscr{P} \rangle \frac{d\mathcal{N}_\gamma}{d\omega'} = \int_0^1 df \langle \mathscr{P} \rangle I_\gamma, \tag{17}$$

where I_γ are given in Eqs. (1) and (2) and the change of variable $\omega' = fE_0$ has been carried out. In the formula above $\langle \mathscr{P} \rangle = \frac{1}{2\delta\phi} \int_{\phi-\delta\phi}^{\phi+\delta\phi} d\tilde{\phi} \mathscr{P}(\tilde{\phi})$ is the pair production probability [see Eq. (15)]:

$$\mathscr{P}(\phi) \approx \int_\Gamma dt dV R(\kappa)|_{\xi \to \xi(\boldsymbol{x},t)} \tag{18}$$

averaged over the collision angle. Hereafter we suppose a deviation $\delta\phi$ due to the spreading of both the decaying gamma quantum and the laser pulse much smaller than ϕ, i.e. $\phi \gg |\delta\phi|$, in which case the approximation $\langle \mathscr{P} \rangle \approx \mathscr{P}$ applies.

Noteworthy, the domain of integration in Eq. (18), i.e. Γ, is defined by the interaction region where the strong field condition $\xi(\boldsymbol{x}, t) \gg 1$ is fulfilled. Observe that for an optical laser with frequency $\omega = 1.55$ eV and peak intensity $I_0 \approx 2 \times 10^{22}$ W/cm^2 (i.e. $\xi = 70$), this translates into $I(\boldsymbol{x}, t)/I_0 \gg 2 \times 10^{-4}$. As Fig. 4 exhibits, this spacetime sector is characterized by oscillations of the strong field modulated by both the focusing and pulse shape functions. Despite the cumbersome form of Γ, the fast damping of $R(\kappa)$ for $\kappa \ll 1$ allows us to extend this domain to the whole interaction region, where the bremsstrahlung beam and laser pulse overlap, without introducing an appreciable error. Indeed, in the presence of a strong pulse, the integration region turns out to be determined by the most separated wavefronts of the bremsstrahlung burst. This requires that in our model the radiation mode with frequency ω' extends over the phase interval $-\frac{1}{2}\omega'\sigma_z \leq k'x \leq \frac{1}{2}\omega'\sigma_z$. In Fig. 4, this restriction translates into a band encompassed between the dashed lines: $z_\pm = -t \pm \frac{1}{2}\sigma_z$. At this point we should stress that the derivation of Eq. (16) relies on a monochromatic plane-wave wave function for the decaying γ quantum. This means that our model assumes the axial σ_z and radial $\bar{r}$ extensions of the bremsstrahlung radiation to substantially exceed the associated wavelength $\lambda' = 2\pi\omega'^{-1}$, which is safely fulfilled.

With all these details to our disposal we find that the scenario where the strong laser field turns out to be described by a paraxial Gaussian pulse (see Sec. II B), the probability can be expressed as

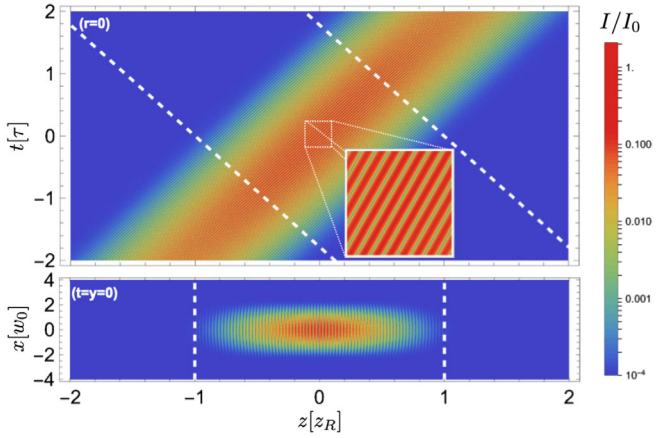

FIG. 4. Behavior of the laser intensity $I(\boldsymbol{x}, t) = E^2(\boldsymbol{x}, t)$ of a paraxial pulse [see Eq. (4)] in t and z (upper panel) and in x and z (lower panel). Here, the dashed lines represent wavefronts of bremsstrahlung radiation separated between each other by a distance $\sigma_z = 2z_R$. The inset of the upper panel reveals the oscillatory feature of the strong field along t and z axes. We have used the same benchmark values and notation as in Table I. For these values and $I_0 \approx 2 \times 10^{22}$ W/cm^2, the strong field condition $\xi(\boldsymbol{x}, t) \gg 1$ translates into $I(\boldsymbol{x}, t)/I_0 \gg 2 \times 10^{-4}$ and $z_R = 15.7$ μm.

$$\mathscr{P} \approx 2\pi \int_{-\infty}^{\infty} dt \int_0^{\infty} r dr \int_{-t-\frac{1}{2}\sigma_z}^{-t+\frac{1}{2}\sigma_z} dz R(\kappa)|_{\xi \to \xi(\boldsymbol{x},t)}, \tag{19}$$

where cylindrical coordinates have been adopted. The combination of Eqs. (17)–(19) with (1) included, constitutes the starting point of our numerical analysis. We note that beyond the paraxial approximation, the cylindrical symmetry of the laser pulse is broken through nontrivial dependences on the azimuthal angle [see Eqs. (B1) and (B2)]. In such a case, the factor 2π in the expression above has to be replaced by an integration over the aforementioned angle.

Next, we consider models in which the strong field background depends only on the phase φ (see Eq. (8) and the discussion that follows it). This scenario can be formulated conveniently via light-cone coordinates: $x_\pm = \frac{1}{\sqrt{2}}(t \pm z)$, $\boldsymbol{x}_\perp = (x, y)$ [59,60]. As a consequence, the strong field phase becomes $\varphi = k_+ x_-$ with $k_+ = (k^0 + k^3)/\sqrt{2} = \sqrt{2}k_0$. In this context, $kk' = k_+ k'_-$, whereas the phase of the gamma quantum $k'x = k'_- x_+$. We note that this set of variables allows us to express the pair production probability as

$$\begin{aligned}\mathscr{P} &= \frac{\omega'}{k_+ k'_-} V_{\rm int} \int_{-\infty}^{\infty} d\varphi R(\kappa)|_{\xi \to \xi(\varphi)} \\ &= -\frac{\alpha m^2}{6\sqrt{\pi} k k'} \frac{V_{\rm int}}{V_\gamma} \int_{-\infty}^{\infty} d\varphi \int_1^{\infty} \frac{du(8u+1)}{u\sqrt{u(u-1)}} \frac{\Phi'(z)}{z}.\end{aligned} \tag{20}$$

Notice that the establishment of the second line required the substitution of Eq. (16) explicitly. As before, $z = (4u/\kappa(\varphi))^{2/3}$ with $\kappa(\varphi) = \kappa|\psi(\varphi)|$. In this expression $V_{\rm int}$ is the interacting volume, the precise form of which depends on the strong field model.[4] Indeed, if the latter turns out to be a plane wave, $V_{\rm int}$ and V_γ coincide and the resulting expression agrees with the outcome resulting from Eq. (33) of Ref. [37]. However, in contrast to our procedure, the expression in the aforementioned reference was obtained from the imaginary part of the vacuum polarization tensor in a plane-wave background via the optical theorem. Now, if the strong pulse is truncated transversally with a size $w_0/\sqrt{2} < \bar{r}$, the interaction volume turns out to be determined by the region occupied by the external field. In this case $V_{\rm int} = A_{\rm int}\sigma_z$ with $A_{\rm int}$ given below Eq. (9), and $V_{\rm int}/V_\gamma \approx w_0^2/(2\bar{r}^2)$, where the result given below Eq. (3) has been used. The ratio between $V_{\rm int}$ and V_γ accounts for the fraction of bremsstrahlung photons that interact with the strong laser pulse and for the parameters assumed in Sec. III amounts to $\approx 2\times 10^{-5}$.

Lastly, if the external field is approximated by $E_x(\varphi) = \mathcal{E}_0\Theta(\frac{1}{2}\Delta\varphi - \varphi)\Theta(\varphi + \frac{1}{2}\Delta\varphi)$, the background turns out to be a constant crossed field. Under such condition the pair creation probability from Eq. (20) reads

$$\mathscr{P} = T_{\rm int}V_{\rm int}R(\kappa) \tag{21}$$

provided the relation $T_{\rm int} = \frac{\tau}{2}\sqrt{\frac{\pi}{\ln(2)}} = \Delta\varphi/(2\omega)$ holds (see below Eq. (9) for $T_{\rm int}$).

Now, the experiment put forward by CALA aims to probe the nonperturbative strong-field regime ($\xi \gg 1$, $\kappa \sim 1$) of the Breit-Wheeler process. In order to elucidate the behavior of R in this limit, we first exploit the relation $\Phi'(z) = -\frac{z}{\sqrt{3}\pi}K_{2/3}(\frac{2}{3}z^{3/2})$ with $K_\nu(x)$ denoting the modified Bessel function of the second kind [47]. As a consequence, Eq. (16) can be written as

$$R = \frac{\alpha m^2}{6\pi\omega' V_\gamma}\frac{8}{3^{3/2}\kappa}\int_{\frac{8}{3\kappa}}^{\infty} dp\,\frac{3\kappa p + 1}{p^{3/2}\sqrt{p - \frac{8}{3\kappa}}}K_{2/3}(p), \tag{22}$$

where the change of variables $p = 8u/(3\kappa)$ has been carried out. For $\kappa \sim 1$ the main contribution in the integral results from the region $p \sim 8/(3\kappa)$. By approximating the integrand with its most slowly decreasing part, we end up with

[4]For a collision geometry other than head-on, $V_{\rm int}$ can depend on the crossing angle ϕ.

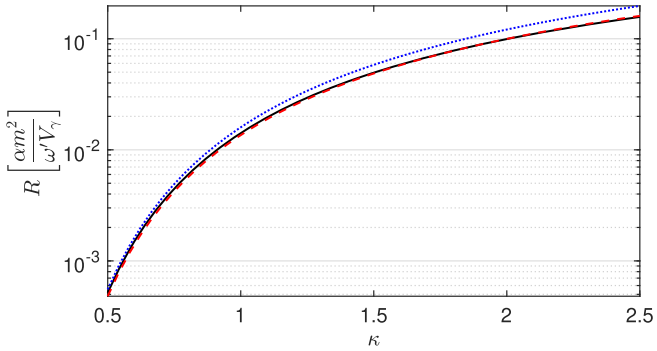

FIG. 5. Comparison of the numerically evaluated rate as given in Eq. (16) (black solid) with the analytical $\kappa \approx 1$ asymptote from Eq. (23) (red dashed) and the limiting case $R_{\kappa\ll 1} \approx \frac{\alpha m^2}{8\omega' V_\gamma}(\frac{3}{2})^{3/2}\kappa e^{-\frac{8}{3\kappa}}$ that is valid for $\kappa \ll 1$ (blue dotted) [4].

$$R_{\kappa\approx 1} \approx \frac{\alpha m^2}{6\pi\omega' V_\gamma}\sqrt{8\kappa}\int_{\frac{8}{3\kappa}}^{\infty} dp\,\frac{K_{2/3}(p)}{\sqrt{p - \frac{8}{3\kappa}}} = \frac{\alpha m^2}{\pi\omega' V_\gamma}\left(\frac{2}{3}\right)^{3/2}K_{7/12}\left(\frac{4}{3\kappa}\right)K_{1/12}\left(\frac{4}{3\kappa}\right). \tag{23}$$

In Fig. 5 we show the behavior of the rate given in Eq. (22) as a function of κ (black solid). For comparison, we have added the rate linked to Eq. (23) in red dashed style and the one corresponding to the case $\kappa \ll 1$ in blue dotted. It is worth remarking that in the region of $\kappa \in [1.5, 2.5]$ the error introduced by Eq. (23) lies below 2% and grows to approximately 10% for $\kappa \ll 1$. This analysis reveals that $R_{\kappa\approx 1}$ provides a good description of the pair production rate for the present study and will be adopted in the forthcoming numerical calculations.

III. RESULTS AND DISCUSSION

A. Comparison of different field models

In this section we use the expressions derived so far to provide estimates for the pair yield by an incident radiating bremsstrahlung electron assuming various laser field models. We shall consider an ideal collision characterized by a perfect synchronization. To avoid longitudinal mismatching, the extension of the bremsstrahlung burst will be chosen so that, at $t = 0$, it covers fully the strong field region of the laser pulse. An examination of Fig. 4 indicates that the conservative value of $\sigma_z = 2z_R \approx 31.4$ μm—which is taken hereafter as a reference parameter—guarantees the previous condition. Observe that the upper bound discussed at the beginning of Sec. II A, i.e. $\sigma_z < \lambda_{\rm p}/(2\pi)$ [41,42], implies that the plasma density has to satisfy the condition $\mathfrak{n}_e < 2.25\times 10^{16}$ cm^{-3} for consigning a monoenergetic witness bunch. We note that this limitation remains within the ballpark $\mathfrak{n}_e < \mathfrak{n}_b$ with $\mathfrak{n}_b \approx 10^{18}$ cm^{-3} established in Ref. [15]. Unless explicitly stated otherwise, we use the

TABLE I. The benchmark parameters envisaged at the experiment to be carried out at CALA in Ref. [15]. These values are adopted hereafter.

Incident electron energy E_0	2.5 GeV
Distance traveled by the bunch L_{e^-}	0.1 m
Incident electrons collimation angle θ_{e^-}	0.5 mrad
Normalized target thickness ℓ	0.015
Distance traveled by bremsstrahlung L	0.5 m
Wavelength of the strong pulse λ	0.8 μm
Pulse waist size w_0	2 μm
Pulse length τ	30 fs
Laser intensity parameter ξ	70
Laser repetition rate	0.1 Hz

benchmark parameters listed in Table I, and a counter-propagating geometry ($\phi = \pi$).

We begin our study by analysing the dependence of the created particle distribution on the bremsstrahlung photon energy. This behavior is summarized in Fig. 6. Depending on the underlying field description, the curves (blue dashed for constant crossed fields (CCF), black solid for pulsed plane wave and red solid for pulsed Gaussian) show the corresponding number of produced pairs. The figure was generated in the following way: for the blue curve we consider only a fraction of the—infinitely extended—field enclosed in the spacetime volume $V_{\rm int}T_{\rm int}$, which contains the same energy as the Gaussian laser pulse [see Eq. (21)]. In the case of the pulsed plane wave we proceed analogously and restrict the spatial components to $V_{\rm int}$. While the constant crossed field description provides the most optimistic prediction, the incorporation of a finite laser duration and a laser focusing diminishes the expected yield by about a factor 5 and 10, correspondingly.

Additionally, all curves in Fig. 6 increase as the energy of bremsstrahlung photons grows meaning that higher energetic photons facilitate the studied pair production process. For the sake of completeness we note that at the right edge of the spectrum the curves should have a maximum at $f \approx 1$ and fall sharply to zero afterwards. This trend is closely linked to the fact that no γ photons can be produced with energy exceeding E_0 and, accordingly, no pairs can be created. The absence of the falling is a result of using the thin target approximation Eq. (1) in N (see Refs. [44,32]). For comparison, Fig. 6 includes a red dotted curve, which results when the thick target approximation in Eq. (2) is applied and a focused Gaussian pulse model adopted. As both red curves lie very close to each other and the contribution of the low energy range $f \in [0, 0.2]$ is negligible we conclude that in the regime of interest, the approximation in Eq. (1) is well applicable and, thus, will be used throughout this study [see discussion below Eq. (2)]. In Fig. 6 we have also contrasted the differential number of pairs resulting from the expressions in Eqs. (16) (blue) and (23) (green dotted). The close overlapping of the curves supports the applicability of the asymptotic formula $R_{\kappa\approx 1}$ in the regime of interest.

The behavior of the expected total number of created pairs as a function of ξ is depicted in Fig. 7. Results stemming from Eq. (21), with the inclusion of (19) and (20) are shown in dashed blue, solid black and solid red, respectively. This figure includes a red dotted curve which has been obtained by setting the collision angle $\phi = 9\pi/10$, as it is planned in the experiment described in Ref. [15]. The corresponding rate has been obtained by performing a rotation of the integration region depicted in Fig. 4. In line, the limitation in the phase of the bremsstrahlung radiation translates into the following limits in z: $z_\pm = -(t \mp \frac{1}{2}\sigma_z)/|\cos(\phi)| + r|\tan(\phi)|$. Observe that the last term may be neglected as long as the longitudinal extension of bremsstrahlung beam is larger than the laser pulse length. We remark that the outlined procedure

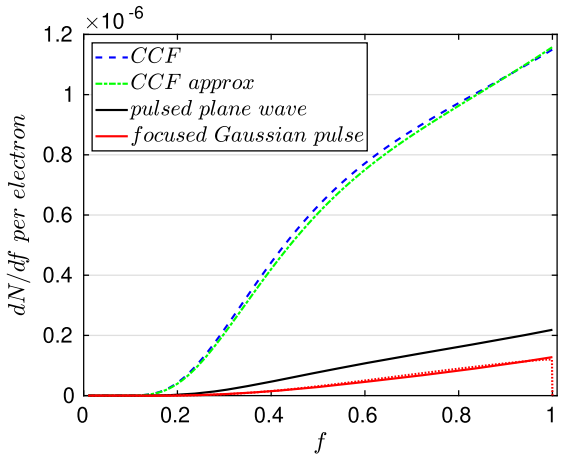

FIG. 6. Differential number of pairs in dependence on the scaled energy of bremsstrahlung photons for $\xi = 70$. We use the same benchmark values and notation as in Table I.

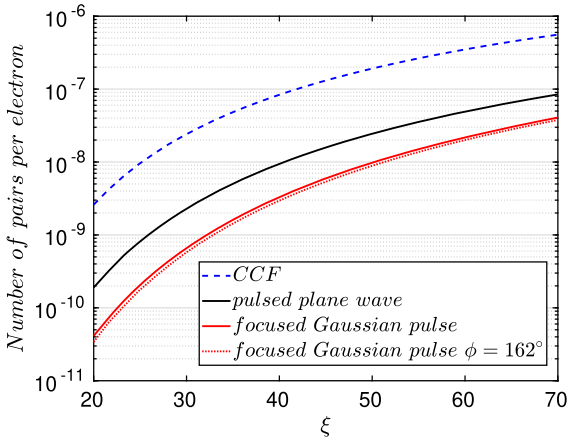

FIG. 7. Pair yield per radiating electron for constant crossed fields (blue dashed), pulsed plane wave (black) and pulsed Gaussian profile (red). The same benchmark parameters and notation of Table I have been used.

represents a good approximation whenever the collision geometry is close to the counterpropagating case.

It can be seen that the incorporation of more realistic field configurations, as it was indicated previously in Fig. 6, modifies the expected outcome by lowering the pair production yield. We remark that the reduction effect originates solely from the laser field description as energy is kept constant for all field shapes (see Sec. II B). While in the case of the constant crossed field the intensity is kept high and constant within the whole interaction spacetime volume [which can be read off from Eq. (7)], the field intensity linked to a Gaussian profile changes from its maximum at the center of the interaction volume to minimal values at its edges. Hence, regardless the consideration of the whole spacetime in the integration of Eq. (18), the intensity gradient has a significant impact on the pair creation yield. The particles are mainly produced in the rather small high-field region close to the focal point—whereas the extended outer regions of the pulse, where the pair production is negligible, still contribute to the pulse energy.

Let us particularize the analysis for $\xi = 70$ which corresponds to an intensity of $I \approx 10^{22}$ W/cm^2. Under such circumstances the expected number of created positrons per incident radiating electron in a single laser shot is 4×10^{-8}. With experimental techniques available nowadays such as laser wake-field acceleration, electron bunches with up to ≈1 nC charge can be generated [61,62]. For an envisaged energy of $E_0 = 2.5$ GeV, we expect bunches of several pC [15]. Therefore, with a 10 pC electron bunch ≈0.03 pairs per laser shot can be observed, if we assume that 1% of incident electrons will emit a bremsstrahlung photon (see discussion in Sec. II A). Hence, when taking into account a laser repetition rate of 0.1 Hz a yield of 10 Breit-Wheeler pairs is expected per hour. This outcome turns out to be much smaller than a prediction reported in Ref. [32], where for $\xi = 30$ up to 10^4 pairs per laser shot and a pC of 2 GeV incident electrons were estimated. However, in contrast to our scenario the prediction given in [32] assumes that the divergence of the bremsstrahlung ray can be counteracted by focusing the incident electron bunch. In our case, the pair yield is reduced by a factor $V_{\rm int}/V_\gamma \sim 10^{-5}$ that results from the beam divergences.

As a next step we analyse, in Fig. 8, the dependence of the pair yield on the thickness of the bremsstrahlung burst. For obtaining the depicted results we modelled the laser as a paraxial Gaussian pulse [see Eq. (4)]. The curve exhibited in this picture shows a downward tendency, which is caused by the longitudinal focusing. Observe that, when the bremsstrahlung bunch is shorter than the laser focal region $2z_R$, more γ photons experience high intensity of the pulse, provided a good synchronization is achieved. On the contrary, for longer bremsstrahlung bunches the contributions from lower intensity regions will decrease the pair yield at the edges of the interaction volume.

B. Contributions from different focal regions

Next, we examine the contributions to the number of pairs stemming from different focal regions. The outcome of this investigation is exhibited in Fig. 9. These curves have been obtained when modelling the laser field as a paraxial Gaussian pulse and changing the integration limits in Eq. (19) to $z \in [-0.75, 0, 75]z_R$, $z \in [-0.5, 0, 5]z_R$, $z \in [-0.25, 0, 25]z_R$, respectively, and $t_\pm = -z \pm \frac{1}{2}\sigma_z$. Here, the patterns in red filled circles, blue open boxes and green open circles manifest the fraction of the pair yield stemming from the reduced integration regions to $z \in [-0.75, 0.75]z_R$, $[-0.5, 0.5]z_R$ and $[-0.25, 0.25]z_R$, respectively. Our assessment reveals that the relative contribution from the innermost region is the higher, the lower the bremsstrahlung photon energy is. This is understandable because, for rather low-energy γ photons, a large value of the laser field is very crucial to yield a sizable pair production signal. However, the major contribution to the

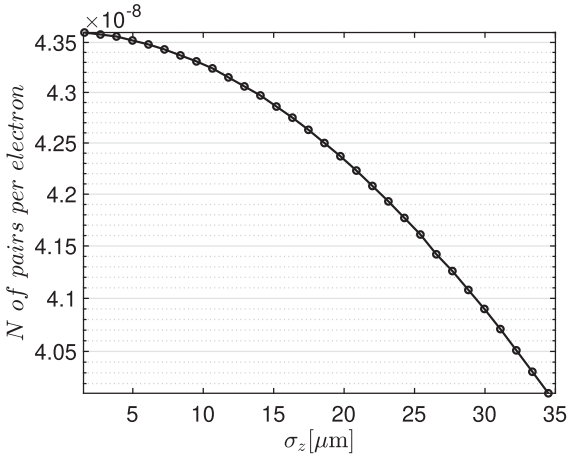

FIG. 8. Dependence of the pair yield on the thickness of the bremsstrahlung bunch σ_z for parameters given in Table I. Moreover, the number of gamma photons in the pulse is kept constant.

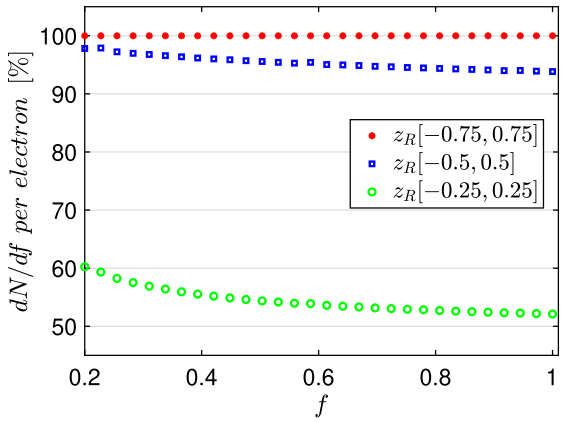

FIG. 9. Differential number of pairs for different branches of focal regions for a focused Gaussian pulse for $\xi = 70$. The other parameters are given in Table I.

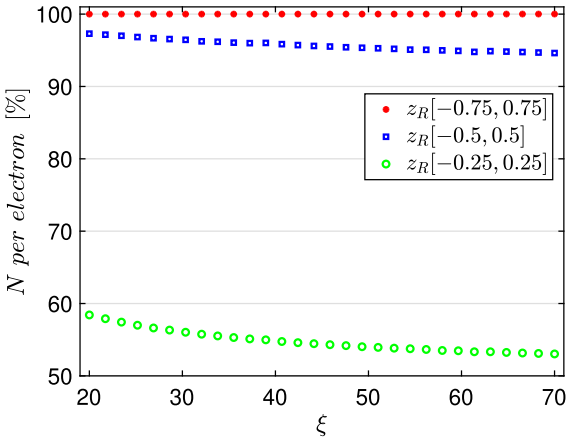

FIG. 10. Percentage of created particles from different focal regions for a focused Gaussian pulse. The other parameters are given in Table I.

total number of pairs stems from high bremsstrahlung energies (see Fig. 6), where the particles are created in the following proportions: while 52% result from $|z| \leq 0.25 z_R$, the doubled region with $|z| \leq 0.5 z_R$ gives 94%, and practically 100% of the pair production is contained in $|z| \leq 0.75 z_R$.

Figure 10 shows how the percentage of the particles produced in different focal regions varies with the laser intensity parameter. Here, we model the laser pulse and change the integration limits as described previously for Fig. 9. The trend exhibited by the curves indicates that with the growing of ξ the importance of the outer zones increases as the high intensity region that facilitates the pair production is extended to the whole Rayleigh length. To be more precise, while the innermost region (green open circles) accounts for about 53% of created pairs for $\xi = 70$, its impact increases to about 58% when the intensity parameter is lowered to 20. This

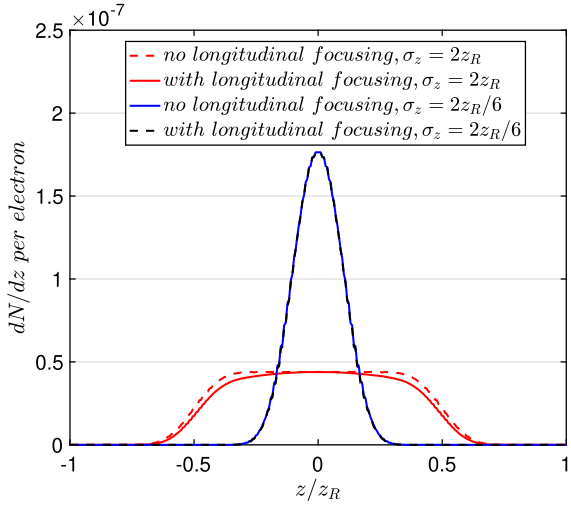

FIG. 11. Distribution of created pairs in the longitudinal direction. We use the same benchmark values and notation as in Table I.

tendency results from the fact that, for rather low ξ, the local quantum nonlinearity parameter κ reaches significant values (close to 1), as required for a sizeable pair production signal, only in the inner focal region. Outside this region, κ quickly falls far below 1 and the pair production is suppressed, accordingly. In contrast, when ξ is large, the local value of κ reaches a sizeable level over a more widespread region where the pair production can occur with significant probability. (Note that the slope of the curves in Fig. 7 decreases with increasing ξ, so that local changes of the field strength in a Gaussian pulse become less crucial when ξ is large.)

A comparison of the distribution of created pairs along the $z-$axis with $\sigma_z = 2z_R$ and $\sigma_z = 2z_R/6$ is shown in Fig. 11. In both cases the dashed curves ignore the longitudinal focusing in the description of the laser field, which is achieved by omitting dependences on $\zeta(z)$ in the paraxial field model in Eq. (4). Conversely, the solid curves incorporate this effect. Also here, the integration in t was limited by $t_\pm = -z \pm \frac{1}{2}\sigma_z$. Observe that the red curves deviate from each other outside the zone $z \in [-0.25, 0.25] z_R$. The outcomes for a shorter bremsstrahlung bunch with $\sigma_z = 2z_R/6$ is shown in blue and black. Here, the effect of the longitudinal focusing is absent as the interaction occurs in the innermost focal region (read the discussion below Fig. 8). Moreover, the larger maximum of the blue curve as compared to the red one at $z = 0$ can be understood as a direct consequence of the shorter bremsstrahlung extension: the number of γ quanta that experiences the region of highest field strength turns out to be larger.

C. Focusing effects

The significance of a wider longitudinal focusing is studied further in Fig. 12, where the ratio between the number of produced pairs linked to models with (N) and without ($N_{z=0}$) longitudinal focusing is exhibited as a

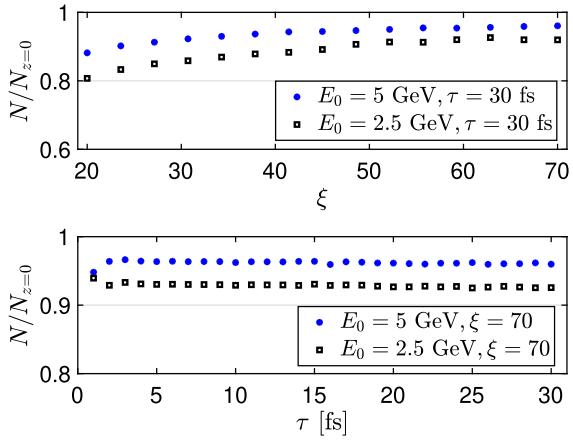

FIG. 12. Dependence of the ratio between the number of produced pairs with (N) and without ($N_{z=0}$) longitudinal focusing on the intensity parameter ξ (upper panel) and the pulse length τ (lower panel). The other parameters are given in Table I.

function of the intensity parameter (upper panel) and the pulse duration (lower panel). In both panels the black and blue dotted curves correspond to $E_0 = 2.5$ GeV and $E_0 = 5$ GeV. However, while the upper panel has been obtained by setting the laser pulse duration to $\tau = 30$ fs, the lower panel follows by setting $\xi = 70$.

On the one hand, the upper panel manifests that the increasing energy of the incident electrons allows us to neglect the longitudinal focusing: for $\xi = 70$ the relative error $1 - N/N_{z=0}$ drops from ∼8% to ∼4%. This tendency, similarly to the effect caused by the intensity, originates in the dependence of κ on the considered parameters (see i.e. Eq. (A3) with $\omega' = fE_0$). When the values of E_0 and ξ are so that $\kappa \approx 1$, the corresponding rate as given in Eq. (23) has a slope less pronounced than in the case where $\kappa \ll 1$ (see also Fig. 5). On the other hand, the curves in the lower panel of Fig. 12 show a plateau for $\tau \gtrsim 3$ fs.

Next, we examine the implication of the transversal laser focusing in more detail. According to Eq. (7), the laser energy $W_G \propto I w_0^2$, where $I = \mathcal{E}_0^2/2$ stands for the average laser intensity. Hence, we can study the impact on the number of pairs yielded by varying simultaneously both the laser intensity I and the beam waist w_0 while keeping W_G constant as achieving higher intensity demands stronger focusing, i.e. narrower beam. This is done by introduction of a scaling factor x for field amplitude and waist size that can be varied without altering the pulse energy:

$$W_G \propto \left(\frac{\xi_0}{x}\right)^2 (w_0 x)^2 = \text{const.} \tag{24}$$

Likewise, the field amplitude can be varied simultaneously with the pulse duration, keeping again W_G fixed.

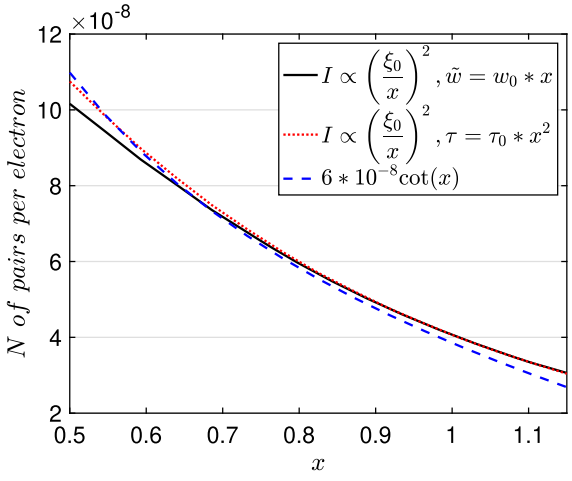

FIG. 13. Impact of focusing when keeping the laser pulse energy constant. Here, the pair yield is maximal for all curves at the smallest considered value $x = 0.5$, which corresponds to the largest intensity parameter $\xi = 2\xi_0$, minimal beam waist $\tilde{w} = w_0/2$ (black) and minimal pulse duration $\tau = \tau_0/4$ (red dotted). The comparison is made for the reference values $\xi_0 = 70$, $w_0 = 2$ μm and $\tau_0 = 30$ fs corresponding to $x = 1$.

The outcome can be seen through the blue curve in Fig. 13 for $w_0 \in [1, 2.3]$ μm and $I \in [0.86, 4.2] \times 10^{22}$ W/cm^2. Here, the smallest value of the beam waist corresponds to the highest intensity. The graph shows a pronounced declining pattern as the intensity decreases gradually while the waist size grows simultaneously. This can be explained because $N \propto \cot(x)$, where x is the proportionality factor that diminishes ξ and increases w_0. The introduction of this parameter encodes two paths to optimize the production of pairs: either by increasing the intensity or by increasing the interaction volume. However, as it can be seen from Fig. 13, the former benefits the process more than the latter in the considered parameter range. Thus, an optimization of the volume quotient V_{int}/V_γ should be achieved by, for example, collimating the incident electron beam with a quadrupole magnet (decreasing θ_{e^-}) or via a faster deflection of electrons which have passed the high-Z target (decreasing L) and not by loose focusing. Observe that the red dotted curve in Fig. 13 depicts the dependence of the yielded pair number on the variations of intensity and pulse duration when keeping the pulse energy constant $W_G \propto I\tau^2$. In analogy to the effect of the beam waist, we see that the consideration of longer pulses at the cost of smaller intensity does not benefit the production of pairs.

By applying a similar procedure as described above, an optimal intensity for the considered setup is found when the incident electron energy is chosen as $E_0 = 10$ GeV. Figure 14 exhibits the maximum at $x \approx 0.9$, which corresponds to $\xi \approx 120$ ($I \approx 3 \times 10^{22}$ W/cm^2) and $\tilde{w} \approx 0.9$ μm. It is worth noting that for $x \lesssim 0.9$, although the strong laser field is more tightly focused, its increased intensity does not guarantee a maximization of the pair production yield. On the contrary, the respective decrease in the interaction

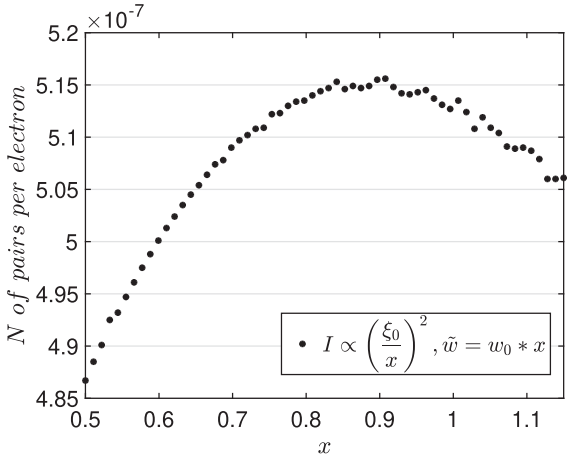

FIG. 14. Number of produced pairs as a function of the laser intensity and the beam waist while keeping the pulse energy constant. The optimal intensity point is found at $x \approx 0.9$, corresponding to $I \approx 3 \times 10^{22}$ W/cm^2 ($\xi = 120$) at $\tilde{w} = 0.9$ μm. The comparison is made for the reference values $\xi_0 = 110$, $w_0 = 1$ μm corresponding to $x = 1$ and $E_0 = 10$ GeV.

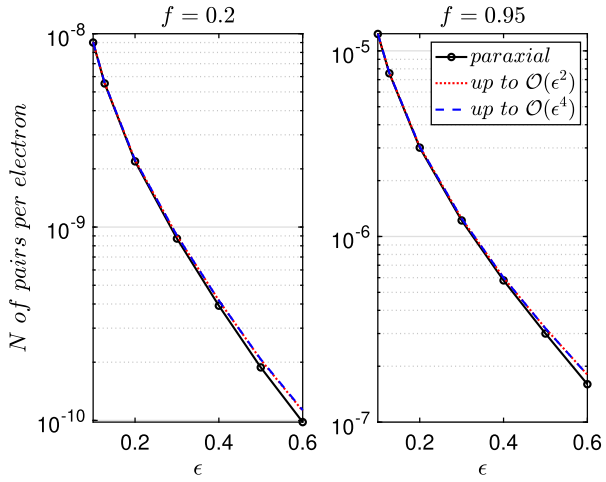

FIG. 15. Deviation in the number of created pairs when considering Gaussian pulse in paraxial approximation (black solid) and beyond paraxial pulses (dotted red and dashed blue) for different diffraction angles ϵ and $\xi = 70$. Here, the energy of incident photons is fixed to $\omega' = 500$ MeV (left panel) and $\omega' = 2.357$ GeV (right panel).

volume outweighs the effect from the increased intensity and results in a shrinking number of created pairs. This study extends the outcome found in Ref. [15], where a similar analysis was carried out for pair production by a monoenergetic γ beam and an intense, not focused laser pulse. As a consequence, the optimal intensity established there was around $I \approx 10^{22}$ W/cm^2 for $\omega' = 2.5$ GeV and $\tilde{w} = 2$ μm.

As it was pointed out previously, the results so far were generated within the paraxial approximation, which is valid as long as the diffraction angle is very small:

$$\epsilon = \frac{2}{w_0 \omega} \ll 1. \tag{25}$$

However, at the points $w_0 = 1$ μm and $w_0 = 0.5$ μm for $\lambda = 0.8$ μm (see Figs. 13 and 14) we reach $\epsilon \approx 0.255$ and $\epsilon \approx 0.51$ correspondingly, which brings the scenario closer to the diffraction limit. Hence, in order to evaluate the extent to which our calculations are well suited, higher order terms in ϵ have been incorporated (see Appendix B). The outcome of this study is summarized in Fig. 15. In this picture, we see the number of created pairs for two particular energies of the bremsstrahlung spectrum, i.e. we do not average over it but rather keep the photon energy constant at 500 MeV (left panel, $f = 0.2$) and 2375 MeV (right panel, $f = 0.95$). In both cases small deviations in the number of created pairs per bremsstrahlung photon start to appear for $\epsilon \gtrsim 0.4$. This fact agrees with the extent of modifications that appear in the electric and magnetic fields at $\epsilon \gtrsim 0.5$ when going beyond the paraxial approximation in Ref. [46], where these fields were initially introduced. Hence, the paraxial approximation is well applicable for the laser parameters envisaged in the present study.

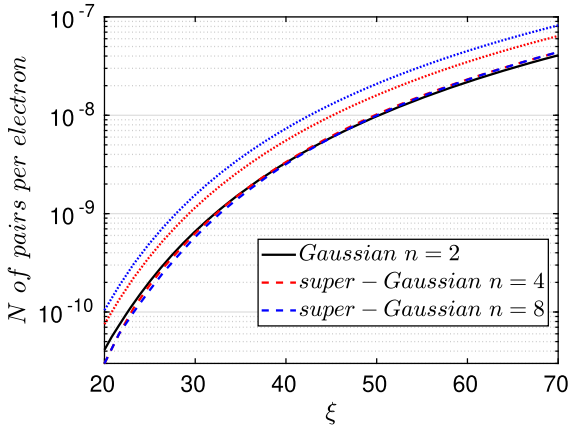

FIG. 16. Number of produced pairs for laser pulses with super-Gaussian time envelopes (red, blue dashed) compared to standard Gaussian with intensity parameter $\xi = 70$ (black solid) when keeping the laser energy at the standard Gaussian level. Dotted curves result when the value of ξ is kept the same for all pulse shapes.

D. Super-Gaussian profiles

We wish to determine the extent to which the results discussed so far are sensitive to the chosen Gaussian time envelope. To evaluate the deviations, we incorporate in the paraxial model [as given in Eq. (4)] a super-Gaussian time profile (see Sec. II B and Fig. 3). These envelopes are characterized by steeper edges and broader plateau regions as contrasted to a standard Gaussian. In order to make a fair comparison we keep the energy of super-Gaussian pulses (exemplarily $n = 4$ and $n = 8$) equal to the standard paraxial pulse. This has been achieved by adjusting the intensities to

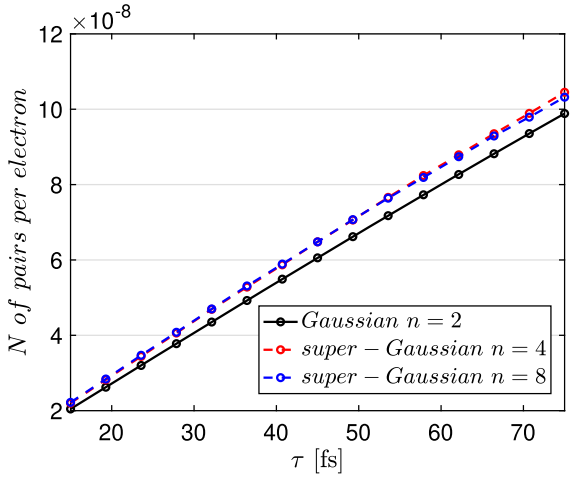

FIG. 17. Number of produced pairs for laser pulses with super-Gaussian time envelopes (red, blue dashed) compared to standard Gaussian (black solid) when keeping the laser energy at the standard Gaussian level. Hence, the intensity parameters read $\xi = 70$ for $n = 2$, $\xi = 63.5$ for $n = 4$ and $\xi = 59.6$ for $n = 8$.

$$I_{n=4} = I\frac{\sqrt{\pi}}{2^{5/4}\Gamma(5/4)} \approx 0.82I,$$
$$I_{n=8} = I\frac{\sqrt{\pi}}{2^{11/8}\Gamma(9/8)} \approx 0.73I, \tag{26}$$

where I stands for the standard paraxial intensity. Thus, we check a standard Gaussian at a particular ξ against super-Gaussian time envelopes with lower effective intensity parameters (as $\xi = \frac{|e|}{m\omega}\sqrt{2I}$). The outcome is depicted in Fig. 16, where the ξ parameter of the standard Gaussian has been varied. Here, the number of created pairs stemming from the latter time profile (solid black line) is compared to super-Gaussians with $n = 4$ (red dashed) and $n = 8$ (blue dashed). While the three curves show an upward trend, the super-Gaussians overpass the pure Gaussian result at $\xi \approx 40$. This agrees with our previous finding that, for relatively lower values of ξ, the pair production is optimized by the highest field intensity, whereas for large ξ values, the process may benefit more strongly from a broadening of the high-field interaction zone. Moreover, the dotted lines in Fig. 16 result from the study, where no modification of the intensity was undertaken. As expected, in this case the super-Gaussians lead to a higher pair yield in the whole intensity range, with the outcome for $n = 8$ exceeding the one for $n = 4$.

Further details are presented in Fig. 17, where the dependence of the pair yield on the pulse duration is shown. Here, as it was done previously the laser pulse energy is kept constant while the field shape is varied by taking a Gaussian with $n = 2$, $\xi = 70$ (black solid) and super-Gaussians with $n = 4$, $\xi = 63.5$ (red dashed) and $n = 8$, $\xi = 59.6$ (blue dashed). While the number of created particles grows with increasing pulse duration for every investigated temporal profile, the broader envelopes lead to a higher pair production yield. Hence, for the considered values of ξ, the effect of increasing the effective interaction time T_{int} over the plateau region [see Eq. (11)] outweighs the decrease in intensity, which was needed to keep the pulse energies equal.

Now, we proceed to study the impact of changing interaction volume when considering super-Gaussian profiles in the transversal focusing. To assess the extent to which the number of produced pairs is modified due to this feature, we adjust their intensities so that the energy carried by these fields coincides with that linked to the standard Gaussian in paraxial approximation. Hence, the corresponding laser intensity parameters turn out to be

$$\xi_{n=4} = \xi(2/\pi)^{1/4} \approx 0.89\xi,$$
$$\xi_{n=8} = \xi(2^{3/4}\Gamma(5/4))^{-1/2} \approx 0.81\xi. \tag{27}$$

At this point, we have varied the $\xi-$ parameter associated with the paraxial model to evaluate the number of yielded pairs. We note that the analytical expression for the super-Gaussians applies only in the $z = 0$ plane, which means that the consequences linked to the longitudinal focusing are ignored. As it has been indicated previously [see Fig. 11], for parameters used in the present study this assumption will not lead to a substantial error. The results of this evaluation are summarized in Fig. 18. Here, the outcome related to a super-Gaussians with $n = 4$ is exhibited in red dashed, whereas the one linked to $n = 8$ appears in blue dashed style. Observe that both curves lie above the black solid curve corresponding to the paraxial result. The effect shown in Fig. 18, although small, provides some hints regarding the importance of optimizing the interaction area: the effect of decreasing the intensity from $I = 10^{22}$ W/cm^2 to $I_{n=4} = 8.4 \times 10^{21}$ W/cm^2 and $I_{n=8} = 6.9 \times 10^{22}$ W/cm^2 may be outweighed by broadening the laser beam. Additionally, Fig. 18 shows dotted curves which describe the number of pairs yielded when the intensity is kept constant for all pulse models. As before, under this condition, the super-Gaussians give larger outcomes than the standard Gaussian throughout, with the pair yield being largest for the super-Gaussian with $n = 8$.

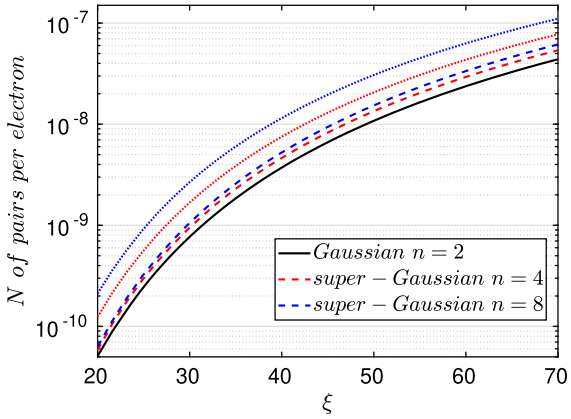

FIG. 18. Number of produced pairs for laser pulses with super-Gaussian spatial envelopes (red, blue dashed) in the transverse plane compared to standard Gaussian with intensity parameter ξ (black solid) when keeping the laser energy at the standard Gaussian level. Dotted curves result when the value of ξ is kept the same for all pulse shapes.

IV. CONCLUSION

Summarizing, we have investigated how the nonlinear Breit-Wheeler pair creation process in the nonperturbative regime with $\xi \gg 1$ depends on the model adopted for describing the strong field of the laser. Our analysis has been focused on a setup which combines highly energetic γ photons produced from bremsstrahlung and a high intensity laser pulse. We have shown that, in such a scenario, an optimization of the yield closely depends on both the laser intensity and the extension of the interaction region.

Throughout the paper we have contrasted the outcomes resulting from different laser field models, including the constant crossed field, the plane-wave and the paraxial Gaussian pulse. This analysis indicates that transversal and

longitudinal focusing of the beam are important features to be taken into account to quantitatively describe upcoming experiments characterized by $\xi \gg 1$ and $\kappa \approx 1$. In order to gain clarity of their role, the percentage of pairs produced in various focal zones along the longitudinal direction has been elucidated. We have shown that, for relatively moderate values of ξ, the majority of particles is produced in the innermost focal region, whereas the contributing interaction zone grows when ξ is increased. Besides, the consequences of broadening the transversal beam profile and the pulse length were investigated separately by adopting super-Gaussian models for the strong laser field. However, this study has revealed no significant difference with respect to the paraxial scenario.

Moreover, the influence of changes in the laser intensity, pulse duration and energy of the incident bremsstrahlung electrons has been considered and the crucial importance of an optimized overlap between the transverse extent of the bremsstrahlung beam and the laser beam waist was emphasized. For the parameters of an envisaged future experiment, relying on incident electrons of $E_0 = 2.5$ GeV energy to generate the bremsstrahlung and laser pulses of 800 nm wavelength, $\xi = 70$ and 30 fs pulse duration [15], we expect the creation of about 0.03 pairs per 10 pC of incident charge and laser shot. This number appears to be resolvable with the advanced detection technologies available nowadays.

ACKNOWLEDGMENTS

This work has been funded by the Deutsche Forschungsgemeinschaft (DFG) under Grant No. 416699545 within the Research Unit FOR 2783/1. The authors thank F. Salgado, K. Grafenstein, D. Seipt, F. Karbstein, J. Farmer and A. Pukhov for useful discussions.

APPENDIX A: TIME AND SPACE DEPENDENT QUANTUM NONLINEARITY PARAMETER

In order to take into account the structure of the strong field we express the quantum nonlinearity parameter $\kappa = |e|\sqrt{-(F_{\mu\nu}k'^{\nu})^2}/m^3$ in terms of the electromagnetic field tensor $F_{\mu\nu}$. As a consequence

$$\kappa = \frac{|e|\omega'\mathcal{E}_0}{m^3}\left[\left(\frac{B_z}{\mathcal{E}_0}\sin(\phi)+\frac{B_y}{\mathcal{E}_0}\cos(\phi)\right)^2+\left(\frac{E_x}{\mathcal{E}_0}\right)^2 + \left(\frac{E_y}{\mathcal{E}_0}\right)^2+\left(\frac{E_z}{\mathcal{E}_0}\right)^2-\left(\frac{E_y}{\mathcal{E}_0}\sin(\phi)+\frac{E_z}{\mathcal{E}_0}\cos(\phi)\right)^2 + 2\frac{B_x}{\mathcal{E}_0}\left(\frac{E_y}{\mathcal{E}_0}\cos(\phi)-\frac{E_z}{\mathcal{E}_0}\sin(\phi)\right)+\left(\frac{B_x}{\mathcal{E}_0}\right)^2 + 2\frac{E_x}{\mathcal{E}_0}\left(\frac{B_z}{\mathcal{E}_0}\sin(\phi)-\frac{B_y}{\mathcal{E}_0}\cos(\phi)\right)\right]^{1/2}, \tag{A1}$$

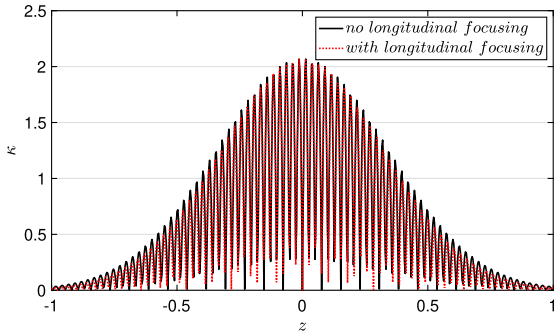

FIG. 19. Local values of the quantum nonlinearity parameter κ for Gaussian pulses with (red dotted) and without (black solid) longitudinal focusing at $t = 0$, $r = 0$.

where E_i and B_i are the electric and magnetic field components, respectively [see Eq. (4)]. Here, ϕ denotes the collision angle, which refers to the z-axis: we assume the geometry, in which the strong laser pulse propagates with the wave vector $\boldsymbol{k} = \omega \boldsymbol{e}_z$ (see Fig. 1).

When the expression above is particularized to the case described in Sec. II B, we end up with

$$\kappa = \frac{|e|\omega'}{m^3}[1-\cos(\phi)]|E_x(t,r,z)|. \tag{A2}$$

In Fig. 19 the dependence of κ on the longitudinal coordinate z is displayed. This picture has been generated by taking into account Eq. (4) with $r = 0$ and $t = 0$. Hence, in the parameter range discussed in this work the local values of κ encompass the interval between 0 and roughly 2. In the limiting case of $w_0 \to \infty$ Eq. (A2) reproduces the formula for the quantum nonlinear parameter in a plane wave background $E_x(t,z) = E_x(\varphi) = E_0\psi(\varphi)$:

$$\kappa_{\mathrm{pw}}(\varphi) = \kappa|\psi(\varphi)|, \tag{A3}$$

where $\kappa = \omega\omega'[1-\cos(\phi)]\xi/m^2$ refers to the standard quantum nonlinearity parameter that arises in calculations dealing with a monochromatic plane wave [37] and the function $\psi(\varphi)$ is defined in Eq. (8).

APPENDIX B: GAUSSIAN PULSE BEYOND PARAXIAL APPROXIMATION

The electric and magnetic fields of a strong Gaussian pulse are modified by higher order contributions in the diffraction angle $\epsilon = w_0/z_R$. According to Ref. [46], up to fourth order they read

$$
\begin{aligned}
E_x &= \mathcal{E}_0 e^{-(\sqrt{2\ln(2)}\frac{(t-z)}{\tau})^2} e^{-\frac{r^2}{w^2(z)}} \left(S_1 + \epsilon^2 \left[\nu^2 S_3 - \frac{\rho^4 S_4}{4} \right] \right. \\
&\quad \left. + \epsilon^4 \left[\frac{S_3}{8} - \frac{\rho^2 S_4}{4} - \frac{\rho^2(\rho^2 - 16\nu^2) S_5}{16} - \frac{\rho^4(\rho^2 + 2\nu^2) S_6}{8} + \frac{\rho^8 S_7}{32} \right] + \mathcal{O}(\epsilon^6) \right), \\
E_y &= \mathcal{E}_0 \nu\eta e^{-(\sqrt{2\ln(2)}\frac{(t-z)}{\tau})^2} e^{-\frac{r^2}{w^2(z)}} \left(\epsilon^2 S_3 + \epsilon^4 \left[\rho^2 S_5 - \frac{\rho^4 S_6}{4} \right] + \mathcal{O}(\epsilon^5) \right), \\
E_z &= \mathcal{E}_0 \nu e^{-(\sqrt{2\ln(2)}\frac{(t-z)}{\tau})^2} e^{-\frac{r^2}{w^2(z)}} \left(\epsilon S_2 + \epsilon^3 \left[-\frac{S_3}{2} + \rho^2 S_4 - \frac{\rho^4 S_5}{4} \right] + \mathcal{O}(\epsilon^5) \right),
\end{aligned} \tag{B1}
$$

$$
B_x = 0, \qquad B_z = \mathcal{E}_0 \eta e^{-(\sqrt{2\ln(2)}\frac{(t-z)}{\tau})^2} e^{-\frac{r^2}{w^2(z)}} \left(\epsilon S_2 + \epsilon^3 \left[\frac{S_3}{2} + \frac{\rho^2 S_4}{2} - \frac{\rho^4 S_5}{4} \right] + \mathcal{O}(\epsilon^5) \right)
$$

$$
B_y = \mathcal{E}_0 e^{-(\sqrt{2\ln(2)}\frac{(t-z)}{\tau})^2} e^{-\frac{r^2}{w^2(z)}} \left(S_1 + \epsilon^2 \left[\frac{\rho^2 S_3}{2} - \frac{\rho^4 S_4}{4} \right] + \epsilon^4 \left[-\frac{S_3}{8} + \frac{\rho^2 S_4}{4} + \frac{5\rho^4 S_5}{16} - \frac{\rho^6 S_6}{4} + \frac{\rho^8 S_7}{32} \right] + \mathcal{O}(\epsilon^6) \right). \tag{B2}
$$

In these formulas $\nu = x/w_0, \eta = y/w_0, \rho^2 = \nu^2 + \eta^2$ and

$$
S_n = \left(\frac{1}{\sqrt{1+\zeta(z)^2}} \right)^n \sin\left[\Phi + (n-1)\, \arctan(\zeta) \right],
$$

$$
C_n = \left(\frac{1}{\sqrt{1+\zeta(z)^2}} \right)^n \cos\left[\Phi + (n-1)\, \arctan(\zeta) \right],
$$

where an explicit expression for Φ can be found in Eq. (5). Moreover, the pulse energy calculated with accuracy up to the fourth order in ϵ reads

$$
W_{\mathrm{BPA}} \approx \frac{\mathcal{E}_0^2}{2} \frac{\pi w_0^2}{2} \left(1 + \frac{\epsilon^2}{4} + \frac{\epsilon^4}{8} \right) \frac{\tau}{2} \sqrt{\frac{\pi}{\ln(2)}}. \tag{B3}
$$

[1] G. Breit and J. A. Wheeler, Collision of two light quanta, Phys. Rev. **46**, 1087 (1934).
[2] H. R. Reiss, Absorption of light by light, J. Math. Phys. (N.Y.) **3**, 59 (1962).
[3] A. I. Nikishov and V. I. Ritus, Quantum processes in the field of a plane electromagnetic wave and in constant field I., Zh. Eksp. Teor. Fiz. **46**, 776 (1963).
[4] A. I. Nikishov and V. I. Ritus, Pair production by a photon and photon emission by an electron in the field of an intense electromagnetic wave and in a constant field, Zh. Eksp. Teor. Fiz. **52**, 1707 (1967).
[5] V. N. Baĭer, A. I. Mil'shteĭn, and V. M. Strakhovenko, Interaction between a photon and an intense electromagnetic wave, Zh. Eksp. Teor. Fiz. **69**, 1893 (1975) [Sov. Phys. JETP **42**, 961 (1976)].
[6] H. R. Reiss, Production of Electron Pairs from a Zero-Mass State, Phys. Rev. Lett. **26**, 1072 (1971).
[7] V. I. Ritus, Quantum effects of the interaction of elementary particles with an intense electromagnetic field, J. Sov. Laser Res. **6**, 497 (1985).
[8] D. L. Burke *et al.*, Positron Production in Multiphoton Light-by-Light Scattering, Phys. Rev. Lett. **79**, 1626 (1997).
[9] J. Adam *et al.* (STAR Collaboration), Measurement of e^+e^- Momentum and Angular Distributions from Linearly Polarized Photon Collisions, Phys. Rev. Lett. **127**, 052302 (2021).
[10] A. Di Piazza, C. Müller, K. Z. Hatsagortsyan, and C. H. Keitel, Extremely high-intensity laser interactions with fundamental quantum systems, Rev. Mod. Phys. **84**, 1177 (2012).
[11] S. Meuren, Probing strong-field QED at FACET-II (SLAC E-320), https://conf.slac.stanford.edu/facet-2-2019/sites/facet-2-2019.conf.slac.stanford.edufiles//basic-page-docs/sfqed2019.pdf.
[12] H. Abramowicz *et al.*, Letter of Intent for the LUXE Experiment, arXiv:1909.00860.
[13] H. Abramowicz *et al.*, Conceptual design report for the LUXE experiment, Eur. Phys. J. Special Topics **230**, 2445 (2021).
[14] C. H. Keitel *et al.*, Photo-induced pair production and strong field QED on Gemini, arXiv:2103.06.059.
[15] F. C. Salgado *et al.*, Towards pair production in the non-perturbative regime, New J. Phys. **23**, 105002 (2021).
[16] T. Heinzl, A. Ilderton, and M. Marklund, Finite size effects in stimulated laser pair production, Phys. Lett. B **692**, 250 (2010).
[17] K. Krajewska and J. Z. Kamiński, Breit-Wheeler process in intense short laser pulses, Phys. Rev. A **86**, 052104 (2012).

[18] A. I. Titov, H. Takabe, B. Kämpfer, and A. Hosaka, Enhanced Subthreshold e+e- Production in Short Laser Pulses, Phys. Rev. Lett. **108**, 240406 (2012); Breit-Wheeler process in very short electromagnetic pulses, Phys. Rev. A **87**, 042106 (2013).
[19] M. J. A. Jansen and C. Müller, Strongly enhanced pair production in combined high- and low-frequency laser fields, Phys. Rev. A **88**, 052125 (2013).
[20] S. Villalba-Chavez and C. Müller. Photo-production of scalar particles in the field of a circularly polarized laser beam, Phys. Lett. B **718**, 992 (2013).
[21] K. Krajewska and J. Z. Kamiński, Coherent combs of antimatter from nonlinear electron-positron-pair creation, Phys. Rev. A **90**, 052108 (2014).
[22] S. Meuren, K. Z. Hatsagortsyan, C. H. Keitel, and A. Di Piazza, Polarization-operator approach to pair creation in short laser pulses, Phys. Rev. D **91**, 013009 (2015).
[23] M. J. A. Jansen and C. Müller, Strong-field Breit-Wheeler pair production in two consecutive laser pulses with variable time delay, Phys. Lett. B **766**, 71 (2017).
[24] A. I. Titov, H. Takabe, and B. Kämpfer, Breit-Wheeler process in short laser double pulses, Phys. Rev. D **98**, 036022 (2018).
[25] Q. Z. Lv, S. Dong, Y. T. Li, Z. M. Sheng, Q. Su, and R. Grobe, Role of the spatial inhomogeneity on the laser-induced vacuum decay, Phys. Rev. A **97**, 022515 (2018).
[26] A. I. Titov and B. Kämpfer, Nonlinear Breit-Wheeler process with linearly polarized beams, Eur. Phys. J. D **74**, 218 (2020).
[27] S. Tang and B. King, Pulse envelope effects in nonlinear Breit-Wheeler pair creation, Phys. Rev. D **104**, 096019 (2021).
[28] Special aspects of Breit-Wheeler pair production are studied in: S. Meuren, K. Z. Hatsagortsyan, C. H. Keitel, and A. Di Piazza, High-Energy Recollision Processes of Laser-Generated Electron-Positron Pairs, Phys. Rev. Lett. **114**, 143201 (2015); M. J. A. Jansen, J. Z. Kamiński, K. Krajewska, and C. Müller, Strong-field Breit-Wheeler pair production in short laser pulses: Relevance of spin effects, Phys. Rev. D **94**, 013010 (2016); T. Nousch, D. Seipt, B. Kämpfer, and A. I. Titov, Spectral caustics in laser assisted Breit-Wheeler process, Phys. Lett. B **755**, 162 (2016); F. Wan, Y. Wang, R. T. Guo, R. R. Chen, R. Shaisultanov, Z. F. Xu, K. Z. Hatsagortsyan, C. H. Keitel, and J. X. Li, High-energy γ-photon polarization in nonlinear Breit-Wheeler pair production and γ polarimetry, Phys. Rev. Research **2**, 032049 (R) (2020); Y. Lu, N. Christensen, Q. Su, and R. Grobe, Space-time-resolved Breit-Wheeler process for a model system, Phys. Rev. A **101**, 022503 (2020); A. Golub, S. Villalba-Chávez, and C. Müller, Strong-field Breit-Wheeler pair production in QED_{2+1}, Phys. Rev. D **103**, 096002 (2021).
[29] A. Di Piazza, Nonlinear Breit-Wheeler Pair Production in a Tightly Focused Laser Beam, Phys. Rev. Lett. **117**, 213201 (2016).
[30] A. Di Piazza, WKB electron wave functions in a tightly focused laser beam, Phys. Rev. D **103**, 076011 (2021).
[31] A. Mercuri-Baron, M. Grech, F. Niel, A. Grassi, M. Lobet, A. Di Piazza, and C. Riconda, Impact of the laser spatio-temporal shape on Breit-Wheeler pair production, New J. Phys. **23**, 085006 (2021).
[32] T. G. Blackburn and M. Marklund, Nonlinear Breit-Wheeler pair creation with bremsstrahlung γ rays, Plasma Phys. Controlled Fusion **60**, 054009 (2018).
[33] A. Hartin, A. Ringwald, and N. Tapia, Measuring the boiling point of the vacuum of quantum electrodynamics, Phys. Rev. D **99**, 036008 (2019).
[34] A. Eckey, A. B. Voitkiv, and C. Müller, Strong-field Breit-Wheeler pair production with bremsstrahlung gamma-rays in the perturbative-to-nonperturbative transition regime, Phys. Rev. A **105**, 013105 (2022).
[35] A. Golub, S. Villalba-Chávez, H. Ruhl, and C. Müller, Linear Breit-Wheeler pair production by high-energy bremsstrahlung photons colliding with an intense x-ray laser pulse, Phys. Rev. D **103**, 016009 (2021).
[36] C. N. Harvey, A. Ilderton, and B. King Testing numerical implementations of strong-field electrodynamics, Phys. Rev. A **91**, 013822 (2015).
[37] A. Di Piazza, M. Tamburini, S. Meuren, and C. H. Keitel, Implementing nonlinear Compton scattering beyond the local-constant-field approximation, Phys. Rev. A **98**, 012134 (2018).
[38] A. Ilderton, B. King, and D. Seipt, Extended locally constant field approximation for nonlinear Compton scattering, Phys. Rev. A **99**, 042121 (2019).
[39] B. King, Uniform locally constant field approximation for photon-seeded pair production, Phys. Rev. A **101**, 042508 (2020).
[40] D. Seipt and B. King, Spin- and polarization-dependent locally-constant-field-approximation rates for nonlinear Compton and Breit-Wheeler processes, Phys. Rev. A **102**, 052805 (2020).
[41] E. Esarey, P. Sprangle, J. Krall, and A. Ting, Overview of plasma-based accelerator concepts, IEEE Trans. Plasma Sci. **24**, 252 (1996).
[42] E. Esarey, C. B. Schroeder, and W. P. Leemans, Physics of laser-driven plasma-based electron accelerators, Rev. Mod. Phys. **81**, 1229 (2009).
[43] M. Lobet, X. Davoine, E. d'Humières, and L. Gremillet, Generation of high-energy electron-positron pairs in the collision of a laser-accelerated electron beam with a multi-petawatt laser, Phys. Rev. Accel. Beams **20**, 043401 (2017).
[44] P. A. Zyla *et al.* (Particle Data Group), Review of Particle Physics, Prog. Theor. Exp. Phys. **2020**, 083C01 (2020).
[45] Y.-S. Tsai, Pair production and bremsstrahlung of charged leptons, Rev. Mod. Phys. **46**, 815 (1974).
[46] Y. I. Salamin, Fields of Gaussian beam beyond paraxial approximation, Appl. Phys. B **86** (2007).
[47] F. W. J. Olver, D. W. Lozier, R. F. Boisvert, and C. W. Clark, *NIST Handbook of Mathematical Functions* (Cambridge University Press, Cambridge, England, 2010).
[48] K. Gillen-Christandl, G. D. Gillen, M. J. Piotrowicz, and M. Saffman, Comparison of Gaussian and super Gaussian laser beams for addressing atomic qubits, Appl. Phys. B **122**, 131 (2016).
[49] M. Santarsiero and R. Borghi, Correspondence between super-Gaussian and flattened Gaussian beams, J. Opt. Soc. Am. A **16**, 188 (1999).
[50] A. Di Piazza, M. Tamburini, S. Meuren, and C. H. Keitel, Improved local-constant-field approximation for strong-field QED codes, Phys. Rev. A **99**, 022125 (2019).

[51] S. S. Bulanov, V. D. Mur, N. B. Narozhny, J. Nees, and V. S. Popov, Multiple Colliding Electromagnetic Pulses: A Way to Lower the Threshold of e^+e^- Pair Production from Vacuum, Phys. Rev. Lett. **104**, 220404 (2010).
[52] A. Fedotov, A. Ilderton, F. Karbstein, B. King, D. Seipt, H. Taya, and G. Torgrimsson, Advances in QED with intense background fields, arXiv:2203.00019.
[53] V. I. Ritus, Radiative effects and their enhancement in an intense electromagnetic field, Zh. Eksp. Teor. Fis. **57**, 2176 (1969) [J. Exp. Theor. Phys. **30**, 1182 (1970)].
[54] N. B. Narozhny, Expansion parameter of perturbation theory in intense-field quantum electrodynamics, Phys. Rev. D **21**, 1176 (1980).
[55] C. Baumann, E. N. Nerush, A. Pukhov, and I. Yu. Kostyukov, Probing non-perturbative QED with electron-laser collisions, Sci. Rep. **9**, 9407 (2019).
[56] T. Podszus and A. Di Piazza, High-energy behavior of strong-field QED in an intense plane wave, Phys. Rev. D **99**, 076004 (2019).
[57] A. Ilderton, Note on the conjectured breakdown of QED perturbation theory in strong fields, Phys. Rev. D **99**, 085002 (2019).
[58] A. A. Mironov, S. Meuren, and A. M. Fedotov, Resummation of QED radiative corrections in a strong constant crossed field, Phys. Rev. D **102**, 053005 (2020).
[59] R. A. Neville and F. Rohrlich, Quantum electrodynamics on null planes and applications to lasers, Phys. Rev. D **3**, 1692 (1971).
[60] W. Becker and H. Mitter, Vacuum polarization in laser fields, J. Phys. A **8**, 1638 (1975).
[61] A. J. Gonsalves *et al.*, Petawatt Laser Guiding and Electron Beam Acceleration to 8 GeV in a Laser-Heated Capillary Discharge Waveguide, Phys. Rev. Lett. **122**, 084801 (2019).
[62] G. Götzfried, A. Döpp, M. F. Gilljohann, F. M. Foerster, H. Ding, S. Schindler, G. Schilling, A. Buck, L. Veisz, and S. Karsch, Physics of Nanocoulomb-Class Electron Beams in Laser-Plasma Wakefields, Phys. Rev. X **10**, 041015 (2020).